

# Imaging standoff detection of explosives using widely tunable midinfrared quantum cascade lasers

**Frank Fuchs**  
**Stefan Hugger**  
**Michel Kinzer**  
**Rolf Aidam**  
**Wolfgang Bronner**  
**Rainer Lösch**  
**Quankui Yang**  
Fraunhofer Institute for Applied  
Solid State Physics  
Tullastraße 72  
79108 Freiburg, Germany  
E-mail: Frank.Fuchs@iaf.fraunhofer.de

**Kai Degreif**  
Fraunhofer Institute for Physical Measurement  
Techniques  
Heidenhofstraße 8  
79110 Freiburg, Germany

**Frank Schnürer**  
Fraunhofer Institute for Chemical Technology  
Joseph-von-Fraunhofer-Straße 7  
76327 Pfinztal, Germany

## 1 Introduction

Increasing public security is a topic of utmost importance for the civil societies all over the world. Therefore, fast and reliable detection of traces of hazardous substances in solid, liquid, or vapor phase is an important issue. A variety of detection techniques have been proposed and demonstrated during the last few years. For cooperative situations that allow sampling close to the object, such as accumulation of air and preparation of well-defined measurement conditions, very high sensitivity can be achieved with state-of-the-art techniques, such as ion-mass spectroscopy and related methods.<sup>1-4</sup> In contrast, standoff measurements on noncooperative objects at safe distance are still a big challenge.<sup>5-11</sup> Because almost all organic chemical compounds exhibit strong characteristic absorbance patterns in the midinfrared spectral range, this task can be addressed with optical methods. Therefore, there is a strong need for compact and robust spectrally tunable infrared radiation sources offering high luminosity and versatility. With quantum cascade (QC) lasers, these demands can be nearly ideally fulfilled. Although impressive progress regarding the spectral tunability has been reported, the spectral tuning range of QC laser-based systems is still an important issue of active research.<sup>12-16</sup>

In this paper, we present the results gained with a mobile imaging standoff detection system comprising an external cavity (EC) QC (EC-QC) laser for spectral selective illumination at infrared wavelengths of  $\sim 7.5 \mu\text{m}$ . We investigated real-world samples such as metal plates covered with

**Abstract.** The use of a tunable midinfrared external cavity quantum cascade laser for the standoff detection of explosives at medium distances between 2 and 5 m is presented. For the collection of the diffusely backscattered light, a high-performance infrared imager was used. Illumination and wavelength tuning of the laser source was synchronized with the image acquisition, establishing a hyperspectral data cube. Sampling of the backscattered radiation from the test samples was performed in a noncooperative geometry at angles of incidence far away from specular reflection. We show sensitive detection of traces of trinitrotoluene and pentaerythritol tetranitrate on real-world materials, such as standard car paint, polyacrylics from backpacks, and jeans fabric. Concentrations corresponding to fingerprints were detected, while concepts for false alarm suppression due to cross-contaminations were presented. © 2010 Society of Photo-Optical Instrumentation Engineers. [DOI: 10.1117/1.3506195]

Subject terms: CBRNE detection; infrared spectroscopy; stand-off detection; remote sensing; infrared laser; quantum cascade laser; external cavity laser.

Paper 100331SSR received Apr. 15, 2010; revised manuscript received Aug. 13, 2010; accepted for publication Sep. 14, 2010; published online Nov. 22, 2010.

standard car paint and backpacks made of polyacrylics (PAs) contaminated with trinitrotoluene (TNT) and pentaerythritol tetranitrate (PETN) in noncooperative geometries. We detect the diffusely backscattered light at arbitrary angles far away from the specular reflection. By spectrally tuning the EC-QC laser across the significant absorption features, we were able to detect surface contaminations of TNT and PETN ranging from  $\sim 20$  to  $200 \mu\text{g}/\text{cm}^2$ . With our detection algorithm, we could suppress signals from potential cross-contaminations of materials with absorption bands in the same spectral region such as flour, hand cream, and cosmetic powder.

## 2 External Cavity Quantum Cascade Laser Source

The key component of the system is a broadly tunable QC laser source. Unlike typical bipolar semiconductor lasers based on interband transitions between conduction and valence band, the emission of a QC laser is generated by intersubband transitions between quantized states in the conduction band. These states are defined by growing an epitaxial structure comprising several hundreds of only a few-nanometers-thick semiconductor layers forming a complex quantum-well structure. Applying band-structure engineering, the gain curve of such a QC laser can be designed according to the specific needs of the application. Our QC lasers are based on  $\text{Ga}_{0.47}\text{In}_{0.53}\text{As}$  quantum wells and  $\text{Al}_{0.48}\text{In}_{0.52}\text{As}$  barriers, which are grown by molecular beam epitaxy lattice matched on InP substrates.<sup>17,18</sup> For the design of the broadly tunable QC laser presented in this paper, we followed Ref. 19. More details on quantum cascade lasers, in general, can be found in Ref. 20.

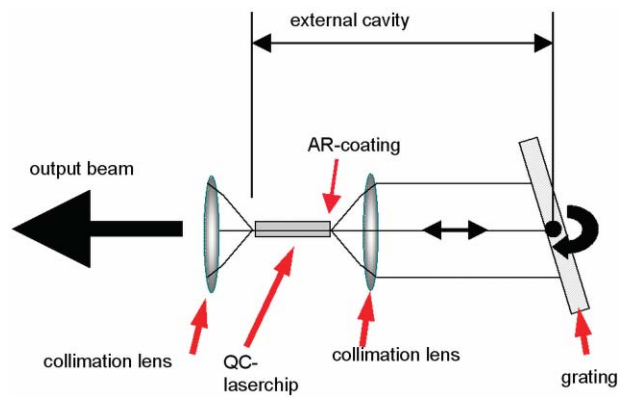


**Fig. 1** Sketch of the external cavity setup in Littrow configuration.

The QC lasers are mounted epitaxial side up on standard Au-coated C-mounts and placed in an external cavity setup in Littrow configuration (see Fig. 1). The front facet is antireflection coated to suppress the internal Fabry–Perot modes of the chip and promote external cavity operation. The residual reflectivity of these coatings is in the range between 0.3 and 1%. The beam is collimated by an aspherical lens and directed toward a blazed diffraction grating, which acts as a spectrally selective cavity mirror. The radiation is coupled out through the back facet, which is left uncoated and acts as the second cavity mirror.

By tuning the angle of the diffraction grating, the emission wavelength of our present QC laser chip can be varied by  $>200\text{ cm}^{-1}$ , corresponding to 15% of the central emission wavelength at  $\sim 7.5\text{ }\mu\text{m}$  (Fig. 2). Because the absorption features to be detected are very broad, we did not aim for single-mode, mode-hopping free tuning of the external cavity laser (ECL) system. Because of the pulsed operation mode, the linewidth of the emission is expected in the range around 100 MHz. In principle, the combination of several active-region designs with different central emission wavelengths into one QC laser-chip (“heterocascading design”) enables a further widening of the tuning range to values exceeding  $400\text{ cm}^{-1}$ .<sup>16</sup>

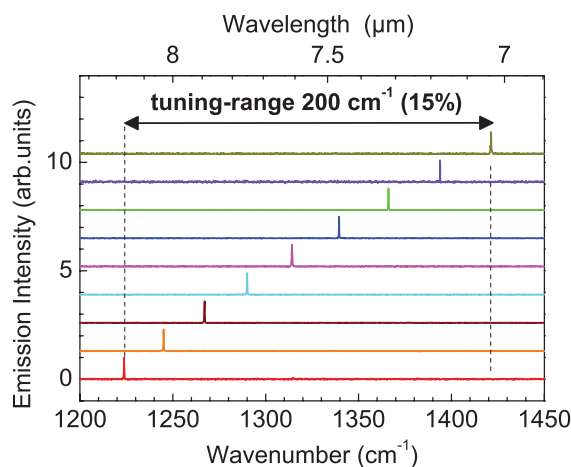


**Fig. 2** Emission spectra of the external cavity laser system comprising a  $15 \times 3500\text{ }\mu\text{m}^2$  QC laser chip. The laser was driven by applying 100-ns pulses with a repetition rate of 10 kHz at 290 K and a current of 4.4 A.

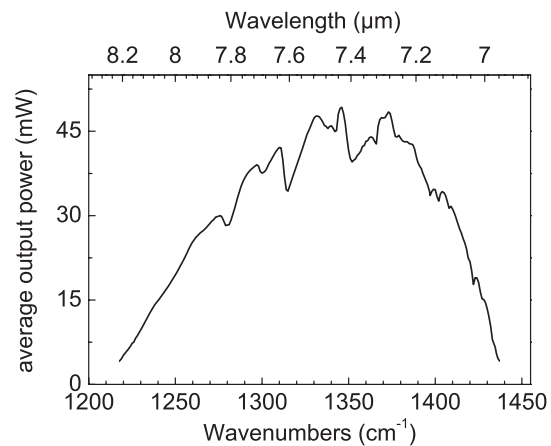


**Fig. 3** Wavelength dependence of the average power of the external cavity laser system comprising a  $15 \times 3500\text{ }\mu\text{m}^2$  QC laser chip. The laser was driven by applying 100 ns pulses with a repetition rate of 1.1 MHz at 290 K corresponding to an 11% duty cycle.

Figure 3 shows the average power of the output beam measured after passing through the outcoupling lens. The laser chip was operated at a heat sink temperature of 290 K by applying 100-ns pulses at a repetition rate of 1.1 MHz, corresponding to a duty cycle of 11%. The spectral structures in the tuning curve are caused by intracavity optical losses partly attributed to the absorption of the collimation lens and the coating materials.

### 3 Mobile Detection System

Figure 4 shows a schematic drawing (a) and a photograph (b) of the whole detection system. It consists of the tunable EC-QC laser module described above, mirror optics for beam guiding with a visible laser pointer incorporated, a “despeckling unit,” a high-performance infrared mercury–cadmium–telluride (MCT) camera, and a visible (VIS) camera. The optical components are positioned on top of a 19-in rack on a rotatable and tiltable stage. The system electronics are placed in the 19-in rack. This system is transportable and can be operated outside a laboratory.

The use of a coherent source for active scene illumination typically leads to the formation of speckle patterns.<sup>21–23</sup> Depending on details of the spatial resolution of the image, these speckle patterns exhibit a spatial noise with root-mean-square (rms) values easily exceeding 50%. Because we have to detect intensity changes in the recorded images on the order of only a few percent, special care has to be taken to avoid this effect. In our setup, the light of the EC-QC laser system passes a set of two polycrystalline diamond plates. One plate is stationary while the second plate is rotating. With this phase scrambler, we achieve a reduction of the spatial rms noise to a level of  $\sim 2\%$ .

After passing the diamond-phase scrambler, the laser light is directed to the surface of interest by conventional beam-forming optics. The diffusely backscattered light from the object is recorded with a  $256 \times 256$  MCT focal-plane array camera with a long-wavelength cutoff at  $10.5\text{ }\mu\text{m}$  and a short-wavelength cut-on defined by a specially designed coldfilter at  $4.2\text{ }\mu\text{m}$ . Because of the special integration mode of the camera (frame rate: 400 Hz, integration time:  $100\text{ }\mu\text{s}$ , duty cycle: 4%) limited by the background photon

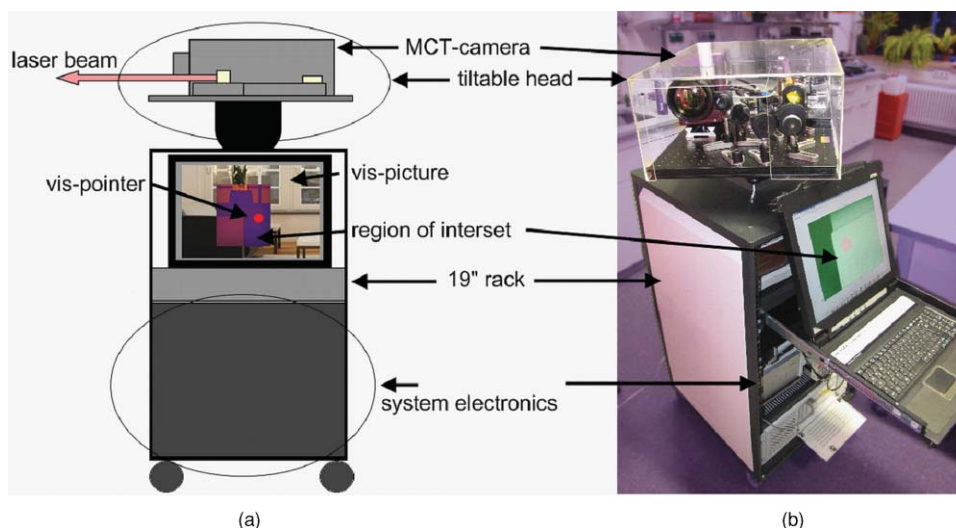


Fig. 4 (a) Schematic of the mobile stand off detection system and (b) photograph of same.

flux of the 300-K scene, the EC-QC laser was driven in a pulse-burst mode. For maximum average output power during the integration period of the camera, bursts of 100- $\mu$ s-long pulses with a burst repetition rate of 400 Hz were applied. Within the pulse burst, the QC laser was driven in short-pulse mode with a 17% duty cycle (100 ns, 1.7 MHz). Recently, we performed a study on the time evolution of the spectral properties of the EC-QC laser.<sup>24,25</sup> This study shows that the emission modes of the external cavity are established within the first 15 ns. The residual intensity of the Fabry-Perot (FP) modes of the quantum cascade laser (QCL) chip at different wavelength die out within 5–10 ns. Thus, 100-ns-long pulses ensure sufficient spectral purity of the laser emission. This operation mode results in a time-averaged duty cycle of <1%, allowing uncooled operation of the laser. With an average laser power during the pulse burst of  $\sim 70$  mW at the center wavelength, the total time-averaged output power is only  $\sim 3$  mW, thus staying well below power levels, at which eye safety becomes an issue. The actual output power emitted by the system is further reduced by the above-mentioned despeckling unit. Therefore, the system's performance can be strongly enhanced in the future by using more powerful lasers without violating the conditions for eye safety, which is of the uttermost importance for the practical applications.

#### 4 Samples

The samples were prepared by deposition of a fingerprint of TNT or PETN on the substrate using a synthetic replicate of a human thumb. This fingerprint leaves no defined concentration on the substrate but more realistically represents the actual residues left by a person handling explosives. The amount of material left on the substrate material is usually between 20 and 200  $\mu$ g/cm<sup>2</sup>. The concentration was estimated by comparison to test samples with well-defined homogeneous distribution of the contamination (not shown). As substrates, we used factory-painted sheets from the autobody sheet of widespread midsize cars (Volkswagen Golf IV and an Opel Astra), PAs, and jeans fabric.

#### 5 Backscattering Spectroscopy

In most practical cases for stand-off trace detection using backscattering (BS) laser spectroscopy, the measurement conditions will differ strongly from a laboratory situation. In the latter case, we typically have an established geometry with well-prepared samples in the measurement chamber of a spectrometer. In contrast, in a real-world scenario the object of interest cannot be configured in a cooperative way. We have to collect the backscattered radiation at arbitrary angles far away from the specular direction. For a better understanding of the hyperspectral data collected with this technique, it is helpful first to examine the simplified case of well-prepared samples. Therefore, in Section 5.1, we first outline detection of traces deposited on man-made samples with a smooth surface exhibiting very low diffuse scattering in the infrared spectral range. We will demonstrate the differences of a highly reflecting surface to a strongly absorbing dielectric surface. In Section 5.2, we outline our approach for handling real-world samples.

##### 5.1 BS Spectroscopy for Simplified Conditions

The simplest case is the detection of a surface coverage of small traces of an explosive on a highly reflecting material, observed under (or close to) specular reflection. We show in Fig. 5 that a contrast can be expected by recording one image by setting the laser wavelength to the absorption band of TNT as the contaminant ("sensing mode") and the second one with the laser wavelength at a spectral position without absorption ("reference mode"). For both images, the thermal background has to be subtracted. Dividing these two data sets yields an image showing the ratio between sensing and reference mode

$$\text{ratio} = \frac{I_{\text{sensing}} \gamma_{\text{scatt}} (1 - \alpha)}{I_{\text{reference}} \gamma_{\text{scatt}}}, \quad (1)$$

Where  $I_{\text{sensing}}/I_{\text{reference}}$  is the QC laser intensity in sensing/reference mode,  $\gamma_{\text{scatt}}$  stands for the percentage of light that is backscattered and  $\alpha$  is the part that is absorbed by the TNT coverage. In this simplified situation, we assume that the scattering efficiencies  $\gamma_{\text{scatt}}$  for the sensing wavelength and the reference wavelength are almost identical and

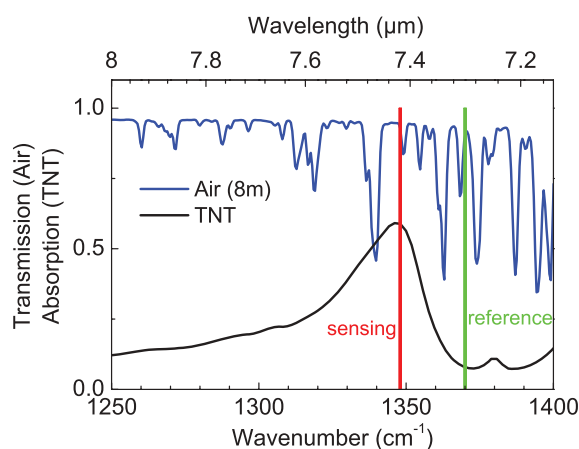


**Fig. 5** Graph of the transmission through air (8 m) and absorption band of TNT measured by applying ATR technique with a FTIR spectrometer. The sensing (red) and reference (green) mode of the system are indicated. (Color online only.)

spectrally flat, which is not necessarily true in real-world samples. In conclusion, the situation described thus far yields a result in agreement with the naive expectation that the reflected intensity will be reduced when the laser is set to a wavelength in the TNT absorption band.

Next, we demonstrate that a thin coverage of TNT on a real-world sample having strong infrared absorbance can cause a contrast reversal. Figure 6 shows measurements of the reflectance of the two types of TNT-covered substrates near normal incidence. The first substrate is an aluminum sheet, representing a highly reflective material as discussed above. The second one is part of an autobody sheet covered with standard car paint, showing strong infrared absorbance. A Bruker Vertex80v Fourier transform-infrared (FTIR) spectrometer was used to conduct the measurements by positioning the samples inside the sample compartment. The

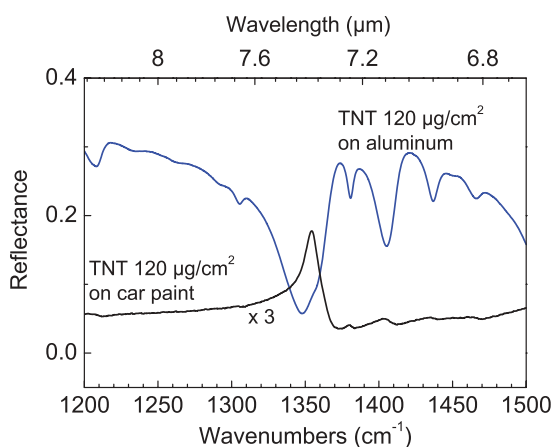


**Fig. 6** Specular reflectance of two different TNT-covered samples with a coverage density of  $120 \mu\text{g}/\text{cm}^2$ . On the aluminum sample offering high-infrared reflectance (blue curve), a reduction of the reflected intensity at the spectral signatures of TNT is observed. In contrast, the same TNT concentration on a highly absorbing layer of car metal paint leads to an inversion of the spectral structures (black curve). Note that the black curve has been multiplied by a factor of 3 for better comparison. Measurements were recorded in a standard reflection setup close to normal incidence in a FTIR spectrometer. (Color online only.)

spectrometer was calibrated with a gold-coated mirror as a reference standard.

The overall level of reflectance decreases to  $\sim 30\%$  when comparing covered Al samples with bare aluminum. This is caused by scattering at the particles of the TNT coverage. Because of the TNT absorption band at  $\sim 1348 \text{ cm}^{-1}$ , the spectral dependence of the measured reflected intensity for the coated samples decreases with a line shape consistent to the measurements of the absorption line of TNT shown in Fig. 5. In the spectral region with high absorbance, the signal decreases.

The measurement on the standard car paint sample covered with TNT leads to completely different results. The overall signal level is much lower. This can be attributed to the high absorbance of the car paint. The coverage of TNT particles on this highly absorbing material leads to a spectral signature, which is inverted compared to the former situation.

A simplified model treating the coverage of TNT particles as a homogeneous thin film on a substrate material enables a quantitative description. Following the theory of Stokes,<sup>26</sup> Bennett<sup>27</sup> et al. offered a formula describing the total reflectance  $\rho_C$  of such a two-layer system,

$$\rho_C = R_C + \frac{T_C^2 R_S}{1 - R_C R_S}, \quad (2)$$

$R_C$ ,  $T_C$  being the reflectance and transmittance of the coating, and  $R_S$  is the reflectance of the bare substrate material. Recently, we demonstrated<sup>28</sup> that for this case the contrast reversal shown in Fig. 6 can be explained by inserting the correct values for the absorbance and reflectance of the combined sample.

## 5.2 Detection for Real-World Conditions

In Section 5.1, we showed two simplified cases for the standoff detection problem using infrared BS spectroscopy. Many real-world materials, as well as the related measurement conditions, are more complex. The surface morphology can be mirrorlike or rough. Typical artificial objects exhibit a smooth surface in the infrared spectral range. Such a surface can be a bare metal, having high infrared reflectance, or a material with high absorbance. A typical example for the latter case is the autobody sheet covered with car paint as outlined in Section 5.1. In a realistic scenario, it is very unlikely that the sample is oriented such that the light originating from specular reflection can be collected. In most cases, only diffusely backscattered light can be observed. On a smooth surface, only the trace contamination itself and other cross contaminations, such as dust, induces light scattering. In such a situation the contamination acts like a source of the backscattered radiation. Thus, the spectral signature of the scattering efficiency of the trace contamination is mixed with the absorbance signature. Materials such as cloth are very efficient diffusers. A trace contamination immersed in such a matrix will be detected via its absorbance properties. A rigorous theoretical description of the spectral properties of these different experimental situations is out of the scope of the present paper and will be described in a future work. A comprehensive overview on the different theoretical approaches describing absorbance in the presence of strong scattering is given in Ref. 29.

An empirical approach for reliable detection of explosives involves the collection of the reference data with the

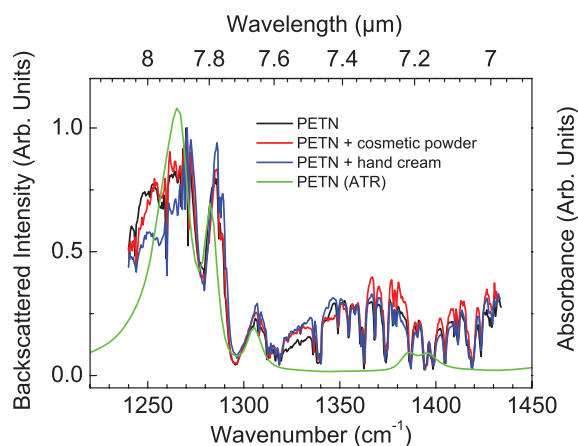


**Fig. 7** Backscattering spectra of PETN with different contamination on a painted autobody sheet, recorded with a resolution of  $0.5 \text{ cm}^{-1}$ . Also shown is an ATR spectrum of PETN (green curve). (Color online only.)

actual system in realistic conditions (i.e., laser illumination and collecting the backscattered light). Spectra of the samples gained with attenuated total reflection (ATR) or from spectroscopic databases, although highly useful to determine the relevant regions providing spectroscopic signatures, can show significant quantitative deviations from what is obtained with our system. To record our reference spectra, the signals from the region in the camera image where the contamination resides was integrated and corrected for thermal background.

Figure 7 shows BS spectra of PETN fingerprints partially mixed with cosmetic powder or hand cream on a painted autobody sheet (Opel Astra) at a distance of 5 m. The spectra are corrected for the wavelength dependence of the laser intensity as measured with a thermopile detector at a close distance to the laser.

Characteristic features are found in the range of  $1240\text{--}1320 \text{ cm}^{-1}$ , unaffected in their spectral positions by the additional presence of cream or powder. The sharp dips for wavenumbers greater than  $\sim 1340 \text{ cm}^{-1}$  are due to atmospheric water absorption. For comparison, we also included an ATR spectrum of a PETN sample. Although similar features appear, their spectral positions are slightly different. The relative intensities of the peaks are different and the BS spectra reside on an additional, slowly varying background. The feature at  $1390 \text{ cm}^{-1}$  appears inverted in the BS spectrum compared to the ATR case. Note also that peaks in the ATR measurements represent absorption, whereas in the case of our detection system peaks correspond to maxima of backscattered intensity. These deviations of the spectral structures on real-world samples in BS configuration to the absorbance spectra recorded in a well-defined ATR configuration are caused by the complicated sample conditions. Besides the effects that can be explained within a multilayer model as outlined in the preceding paragraph, the main difference lies in the fact that in the the sample acts both as an absorber as well as a scattering source in the BS case.

In Fig. 8, the corresponding spectra for TNT on autobody sheet are presented, measured at a distance of 2 m. The most obvious feature is the large drop in intensity from  $\sim 1320 \text{ cm}^{-1}$  to an absolute minimum at  $1365 \text{ cm}^{-1}$ . The differences to the ATR measurement, which nevertheless indi-

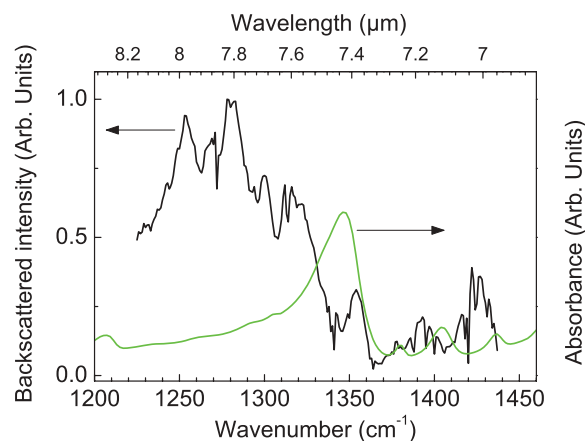


**Fig. 8** Backscattering spectroscopy of a TNT fingerprint on autobody sheet, recorded with a resolution of  $1 \text{ cm}^{-1}$  (black) and the corresponding ATR measurement (green). (Color online only.)

cates the relevant spectral region, are even more pronounced than in the PETN case.

Summarizing these spectroscopic investigations, we conclude that a full theoretical description of the expected spectra will be very difficult.<sup>29</sup> We have to expect that one type of explosive will exhibit a limited variety of spectral signatures. The true signature of the individual measurement depends on the surface conditions. For the current application, we choose an empirical approach. The spectroscopic data set for the detection has to be established for a variety of real-world conditions with a BS setup close to the final system.

## 6 Imaging Detection of TNT and PETN

In this section, we present results on the imaging detection of fingerprints of TNT and PETN in the presence of different cross contaminations on substrates that are likely to be relevant in a real-world application. Imaging detection represents an important step forward compared to spectroscopic investigations with a single-element detector (i.e., integration of the whole backscattered intensity). Not only does the imaging approach provide visualization and localization of contaminated areas on the object under consideration, it can also give a better signal-to-noise ratio. In future applications, a large part of a given object will be illuminated. If the total backscattered intensity is integrated without spatial resolution, then the signal from the contamination, originating only from a small fraction of the total illuminated area, will be embedded in a large background. This is not the case in the imaging approach, where contributions from different sample areas are investigated separately. In principle, spectroscopy can be carried out on every single pixel of the camera detector.

Here, we used a limited set of illumination wavelengths based on the reference spectra shown above. For automatic detection, at the present stage of the work we applied the simple two-point mode outlined above (i.e., division of two background-corrected images taken at different wavelengths). By defining a threshold on the ratio image, the system identifies the contaminated spots. In the future, a more sophisticated algorithm based on multivariate analysis will be applied. Typically, a large part of the sample plate of  $10 \times 10 \text{ cm}^2$  in size was illuminated. The plate was tilted to angles of  $>20 \text{ deg}$  off the specular direction. Thus, only the diffusive fraction of the backscattered light was recorded.

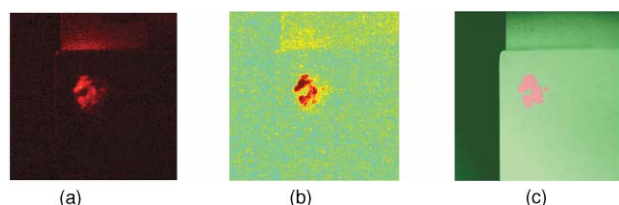


**Fig. 9** Images produced by the detection algorithm. (a) Active illumination, sensing channel (thermal contribution subtracted), (b) ratio of sensing ( $1320\text{ cm}^{-1}$ ) channel and reference channel ( $1370\text{ cm}^{-1}$ ), and (c) thermal image of the object (green). TNT detected parts are colored in red for alert. (Color online only.)

Distances were  $\sim 2\text{ m}$ , limited mainly by the available laser power.

Figure 9 shows the detection of a fingerprint of TNT on the autobody sheet from a Volkswagen Golf IV covered with standard car paint. Figure 9(a) shows the raw data obtained in the sensing channel after subtraction of the passive infrared image. In fig. 9(b) the ratio of sensing to reference channel is given. A clear signature is observed. Figure 9(c) shows the detected TNT contamination in red after image processing, using a threshold for discrimination. The distribution of detected TNT is fused as a red alarm region into the passive infrared image.

In Fig. 10, we illuminated four fingerprints ( $3 \times$  PETN,  $1 \times$  cosmetic powder) on an autobody sheet (Opel Astra) optically looking similar to five wavelengths suitable to obtain the characteristic PETN features from Fig. 7. The backscattered intensity of the PETN traces follows the expected maximum/minimum sequence, allowing unambiguous identification and localization of the traces within the illuminated area of the sample. For automatic detection, we again used the simple two-point algorithm outlined in Section 5.1, with  $1287\text{ cm}^{-1}$  acting as sensing and  $1296\text{ cm}^{-1}$  as reference channel.

Figure 11 demonstrates the ability to discriminate between different substances. Traces of PETN and TNT were illuminated simultaneously. Although in both cases there is a rather high intensity at  $1287$  and  $1307\text{ cm}^{-1}$ , the strong reduction of scattering at  $1296\text{ cm}^{-1}$  (specific for PETN) and  $1366\text{ cm}^{-1}$

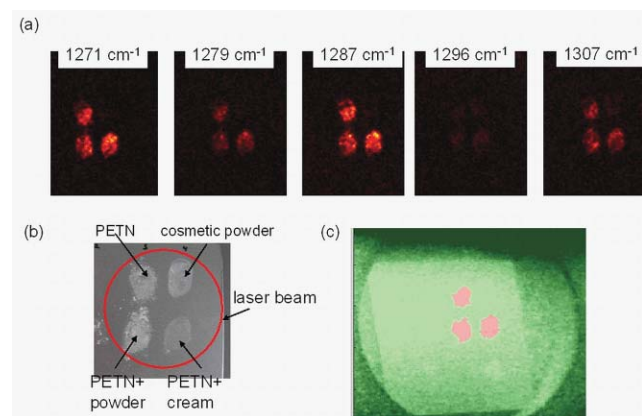


**Fig. 10** (a) PETN on autobody sheet (Opel Astra) illuminated at different wavelengths chosen to reveal characteristic spectral features of PETN, (b) sample, and (c) thermal image of the object. PETN detected parts are colored in red for alert. (Color online only.)

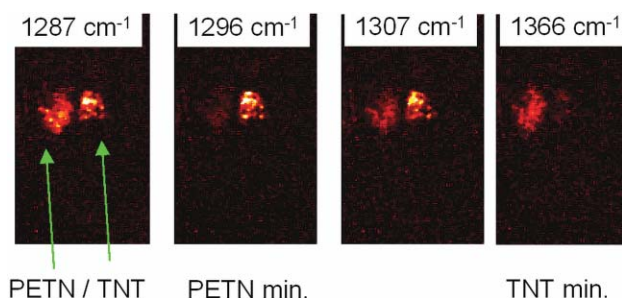


**Fig. 11** A suitable set of illumination wavelengths allows a clear discrimination between different substances of interest, as shown here for the case of PETN and TNT on an autobody sheet. Although both substances show a significant BS intensity (e.g., at  $1287\text{ cm}^{-1}$ ), the minima at  $1296\text{ cm}^{-1}$  (PETN) and  $1366\text{ cm}^{-1}$  (TNT) are characteristic for the respective explosive.

(TNT) allows us to clearly distinguish between these two explosives.

As a final example, Fig. 12 shows a fingerprint of PETN (mixed with hand cream) on PAs, a material used, e.g., for the outer shell of a backpack. Again, we find the very pronounced intensity difference between  $1287$  and  $1296\text{ cm}^{-1}$ . Contrary to the autobody sheets investigated thus far, PAs show noticeable diffuse scattering of laser light. Therefore, the PETN region appears darker than its surrounding at an illumination wavelength of  $1296\text{ cm}^{-1}$ . Again, the two-point detection algorithm indicates the presence of PETN. Similar results were obtained with TNT on PA as well as with PETN and TNT on jeans fabric.

As seen in Fig. 11, the characteristic spectral features of TNT and PETN allow a clear discrimination between the two substances. In order to evaluate the sensitivity to the false alarm of our system, we performed further measurements on nonhazardous materials that typically contaminate the surface when the object is handled. Flour and cosmetic powder are substances that visually look very similar to a TNT contamination on a surface (see Fig. 12). Figure 13 shows spectra of cosmetic powder and flour on PAs. These spectra are

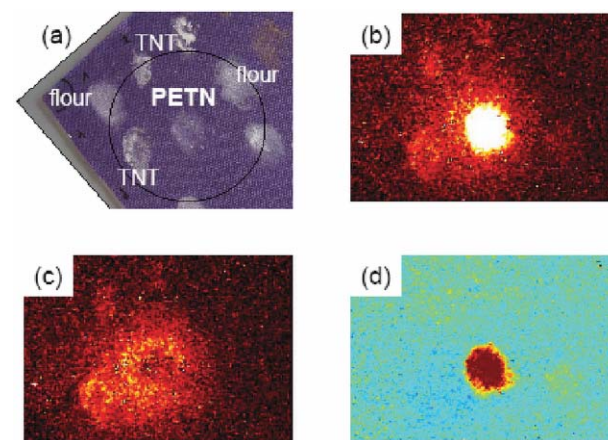


**Fig. 12** (a) Visible image of a PAs sample with a fingerprint of PETN. The circle indicates the illumination by the laser beam. (b) Illumination at  $1287\text{ cm}^{-1}$ , thermal background subtracted; (c) illumination at  $1296\text{ cm}^{-1}$ , thermal background subtracted. The PETN-contaminated area appears darker than the surrounding PAs. (d) Ratio of  $1287\text{ cm}^{-1}/1296\text{ cm}^{-1}$  providing clear contrast due to the presence of PETN.

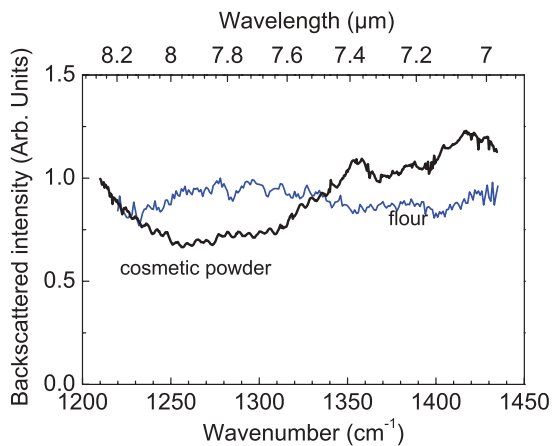


**Fig. 13** Spectrum of powder (Penaten) and flour on PAs, divided by the spectrum measured directly on PAs.

divided by the spectrum of the substrate material, measured spatially close to the contamination. With this approach, the optical path of the signal and reference wavelength is identical. Therefore, the signatures of water absorption seen in the spectra shown in Fig. 7 cancel out. Cosmetic powder exhibits a reduced backscattered intensity in the right part of the investigated spectral region with a very broad minimum  $\sim 1270 \text{ cm}^{-1}$ , while flour shows only minor intensity variations. In both cases, there is a clear difference to TNT or PETN in the spectral region of interest. Therefore, with the present approach using the spectral signatures for detection, a low false alarm rate can be expected for these cross contaminations.

## 7 Summary and Outlook

An imaging standoff detection system for hazardous materials is presented. The external cavity laser in the system enables BS laser spectroscopy in the third atmospheric window covering a tuning range of  $\sim 200 \text{ cm}^{-1}$ , corresponding to 15% of the midinfrared spectral region. As an example, the detection of fingerprints of TNT and PETN on real-world car plates have been demonstrated. The suppression of false alarms due to other contaminants is possible. We showed that the spectral signature of explosives strongly depends on the experimental situation. The spectroscopic database of a final system must include these different cases. A sophisticated algorithm will be needed for efficient evaluation of the hyperspectral data cube. The technique uses harmless radiation in the thermal infrared and therefore enables concealed observation. The laser power needed for the active illumination is eye safe.

A detection system with an operation distance of a few meters will be suitable for the screening of bags or suitcases at public places such as airports or train stations. However, it is clear that any detection system aiming, e.g., at vehicle-based bombs must be capable to operate at much larger standoff distances. There are several ways to bring our system to higher sensitivity and larger detection distances. Because we detect the diffusely backscattered radiation of a collimated beam, the intensity drop with increasing distance follows an inverse square law. Recent progress in the development of high-power QC lasers with  $\lambda \sim 4.6 \mu\text{m}$  has led to devices with a maximum continuous wave (CW) output power of

3 W at room temperature.<sup>30</sup> Furthermore, by polarization coupling of two QC lasers, the output power can be further scaled up while preserving the original beam quality. Therefore, it is safe to assume that QC laser modules with 1-W output power will be available in the near future also for  $\lambda \sim 8 \mu\text{m}$ , corresponding to an enhancement of a factor of  $\sim 20$  compared to the EC-QC laser module used in this study. Furthermore, the optical throughput of the present despeckling unit and the following collimation optics is still low and may be enhanced by a factor of 3. By increasing the diameter of the optics of the collection aperture from the present value of 4–12.5 in. of a tele-optics, a factor of 9 is gained. Combining all these improvements, we estimate a gain of the detection distance of an optimized system by a factor of  $\sqrt{20 \cdot 3 \cdot 9} > 20$ . Consequently, we expect that measurement distances between 20–50 m are feasible within our approach.

## Acknowledgments

The authors thank K. Schäuble, K. Schwarz, U. Weinberg, A. Michailov, and R. Moritz for expert technical assistance and B. Raynor for careful reading of the paper. We appreciate the encouraging support of J. Wagner. The work has been supported by the German Ministry for Education and Research (BMBF) through the project IRLDEX.

## References

- C. Bauer, A. K. Sharma, U. Willer, J. Burgmeier, B. Braunschweig, W. Schade, S. Blaser, L. Hvozdar, A. Müller, and G. Holl, "Potentials and limits of mid-infrared laser spectroscopy for the detection of explosives," *Appl. Phys. B* **92**(3), 327–333 (2008).
- R. Orghici, U. Willer, M. Gierszewska, S. R. Waldvogel, and W. Schade, "Fiber optic evanescent field sensor for detection of explosives and CO<sub>2</sub> dissolved in water," *Appl. Phys. B* **90**(2), 355–360 (2008).
- I. Dunayevskiy, A. Tsekoun, M. Prasanna, R. Go, and C. K. N. Patel, "High-sensitivity detection of triacetone triperoxide (TATP) and its precursor acetone," *Appl. Opt.* **46**(25), 6397–6404 (2007).
- T. J. Cornish, M. D. Antoine, S. A. Ecelberger, and P. A. Demirev, "Arrayed time-of-flight mass spectrometry for time-critical detection of hazardous agents," *Anal. Chem.* **77**(13), 3954–3959 (2005).
- C. W. van Neste, L. R. Senesac, and T. Thundat, "Standoff photoacoustic spectroscopy," *Appl. Phys. Lett.* **92**(23), 234102 (2008).
- R. Furstenberg, C. A. Kendziora, J. Stepnowski, S. V. Stepnowski, M. Rake, M. R. Papantonakis, V. Nguyen, G. K. Hubler, and R. A. McGill, "Stand-off detection of trace explosives via resonant infrared photothermal imaging," *Appl. Phys. Lett.* **93**, 224103 (2008).
- R. Harig, R. Braun, C. Dyer, C. Howle, and B. Truscott, "Short-range remote detection of liquid surface contamination by active imaging fourier transform spectrometry," *Opt. Express* **16**(8), 5708–5714 (2008).
- R. E. Hummel, A. M. Fuller, C. Schollhorn, and P. H. Holloway, "Detection of explosive materials by differential reflection spectroscopy," *Appl. Phys. Lett.* **88**(23), 231903 (2006).
- M. B. Pushkarsky, I. G. Dunayevskiy, M. Prasanna, A. G. Tsekoun, R. Go, and C. K. N. Patel, "High sensitivity detection of TNT," *Proc. Nat. Acad. Sci. USA* **103**(52), 19630–19634 (2006).
- M. Gaft and L. Nagli, "Standoff laser based spectroscopy for explosives detection," *Proc. SPIE* **6739**, 673903 (2007).
- S. Wallin, A. Petterson, H. Östmark, and A. Hobro, "Laser-based stand-off detection of explosives: a critical review," *Analyt. Bioanal. Chem.* **395**(2), 259–274 (2009).
- R. Maulini, A. Mohan, M. Giovannini, J. Faist, and E. Gini, "External cavity quantum-cascade laser tunable from 8.2 to 10.4  $\mu\text{m}$  using a gain element with a heterogeneous cascade," *Appl. Phys. Lett.* **88**, 201113 (2006).
- B. G. Lee, M. A. Belkin, R. Audet, J. MacArthur, L. Diehl, C. Pflügl, F. Capasso, D. C. Oakley, D. Chapman, A. Napoleone, D. Bour, S. Corzine, G. Höfler, and J. Faist, "Widely tunable single-mode quantum cascade laser source for mid-infrared spectroscopy," *Appl. Phys. Lett.* **91**, 231101 (2007).
- G. Wysocki, R. Lewicki, R. F. Curl, F. K. Tittel, L. Diehl, F. Capasso, M. Troccoli, G. Höfler, D. Bour, S. Corzine, R. Maulini, M. Giovannini, and J. Faist, "Widely tunable mode-hop free external cavity quantum cascade lasers for high resolution spectroscopy and chemical sensing," *Appl. Phys. B* **92**(3), 305–311 (2008).
- R. Maulini, I. Dunayevskiy, A. Lyakh, A. Tsekoun, C. K. N. Patel, L. Diehl, C. Pflügl, and F. Capasso, "Widely tunable high-power external

- cavity quantum cascade laser operating in continuous-wave at room temperature,” *Electron. Lett.* **45**(2), 107–108 (2009).
16. A. Hugi, R. Terazzi, Y. Bonetti, A. Wittmann, M. Fischer, M. Beck, J. Faist, and E. Gini, “External cavity quantum cascade laser tunable from 7.6 to 11.4  $\mu\text{m}$ ,” *Appl. Phys. Lett.* **95**, 061103 (2009).
  17. F. Fuchs, B. Kim, C. Mann, Q. Yang, W. Bronner, B. Raynor, K. Köhler, and J. Wagner, “Spectral tuning and mode competition in quantum cascade lasers studied by time-resolved Fourier transform spectroscopy,” *Proc. SPIE* **6386**, 63860I (2006).
  18. B. Hinkov, F. Fuchs, W. Bronner, K. Köhler, and J. Wagner, “Current- and temperature-induced beam steering in 7.8  $\mu\text{m}$  emitting quantum-cascade lasers,” *J. Quantum Electron.* **44**(11), 1124–1128 (2008).
  19. J. Faist, M. Beck, and T. Aellen, “Quantum-cascade lasers based on a bound-to-continuum transition,” *Appl. Phys. Lett.* **78**(2), 147–149 (2001).
  20. C. Gmachl, F. Capasso, D. L. Silvieo, and A. Y. Cho, “Recent progress in quantum cascade lasers and applications,” *Rep. Prog. Phys.* **64**, 1533–1601 (2001).
  21. S. Lowenthal and D. Joyeux, “Speckle removal by a slow moving diffuser associated with a motionless diffuser,” *J. Opt. Soc. Am.* **61**, 847–851 (1971).
  22. J. W. Goodman, “Speckle phenomena, in *Optics: Theory and Applications*, Roberts and Co., Greenwood Village, CO (2007).
  23. S. An, A. Lapchuk, V. Yurlov, J. Song, H. W. Park, J. Jang, W. Shin, S. Kargapoltsev, and S. K. Yun, “Speckle suppression in layer-display using several partially coherent beams,” *Opt. Express* **17**, 92–103 (2009).
  24. B. Hinkov, Q. Yang, F. Fuchs, W. Bronner, K. Köhler, and J. Wagner, “Time-resolved characterization of external-cavity quantum-cascade lasers,” *Appl. Phys. Lett.* **94**(22), 221105 (2009).
  25. Q. K. Yang, B. Hinkov, F. Fuchs, W. Bronner, K. Köhler, J. Wagner, R. Maulini, and J. Faist, “Rate equations analysis of external-cavity quantum cascade lasers,” *J. Appl. Phys.* **107**, 043109 (2010).
  26. G. D. Stokes, “On the intensity of the light reflected or transmitted through a pile of plates,” *Proc. R. Soc. London* **11**, 545–557 (1860).
  27. J. M. Bennett, E. Pelletier, G. Albrand, J. P. Borgogno, B. Lazarides, C. K. Carniglia, R. A. Schmell, T. H. Allen, T. Tuttle-Hart, K. H. Guenther, and A. Saxer, “Comparison of the properties of titanium dioxide films prepared by various techniques,” *Appl. Opt.* **28**(16), 3303–3317 (1989).
  28. B. Hinkov, F. Fuchs, J. M. Kaster, Q. Yang, W. Bronner, R. Aidam, and K. Köhler, “Broad band tunable quantum cascade lasers for stand-off detection of explosives,” *Proc. SPIE* **7484**, 748406 (2009).
  29. B. Philips-Inversizzi, D. Dupont, and C. Case, “Bibliographical review for reflectance of diffusing media,” *Opt. Eng.* **40**, 1082–1092 (2001).
  30. A. Lyakh, R. Maulini, A. Tsekoun, R. Go, C. Pflügl, L. Diehl, Q. J. Wang, F. Capasso, and C. K. N. Patel, “3 W continuous-wave room temperature single-facet emission from quantum cascade lasers based on nonresonant extraction design approach,” *Appl. Phys. Lett.* **95**, 141113 (2009).

Biographies and photographs of the authors not available.